

Liquid sloshing behaviours in an elastic tank and suppression effect of baffles

Chenxi Zhao^a, Yan Wu^a, Yongchuan Yu^a, Oskar J. Haidn^a, Xiangyu Hu^{b,*}

^aChair of Space Propulsion and Mobility, Technical University of Munich, 85521 Ottobrunn, Germany

^bChair of Aerodynamics and Fluid Mechanics, Technical University of Munich, 85748 Garching, Germany

Abstract

In this paper, a fluid-structure interaction (FSI) framework based on the smoothed particle hydrodynamics (SPH) method is employed to investigate the forces and deformations experienced by LNG tanks during liquid sloshing. As a Lagrangian approach, the SPH method offers the advantage of accurately modelling free-surface flow. The fluid phase consisting of water and air is modelled as a multi-phase system for getting closer to real transport situations. Additionally, the application of FSI within a single framework reduces data transfer discrepancies between fluid dynamics and solid mechanics. To validate the reliability of the numerical methodology, the simulation results about the free surface elevation and wave profiles are compared with experimental data. Subsequently, ring baffles and vertical baffles are introduced separately. While the degree of force acting on the tanks is assessed, the anti-sloshing effectiveness of baffles on sloshing suppression and the variations in stress and strain distributions are evaluated. Further, to compare the influence of the material properties of baffles on sloshing phenomena, the rigid baffle and elastic baffle with different Young's moduli are immersed in the liquid. The results indicate that in this LNG tank configuration, the closer the baffle properties align with rigidity, the more effective the sloshing inhibition.

Keywords: Tank sloshing, SPH, FSI, deformable structure, multi-phase flow

1. Introduction

Liquefied natural gas (LNG), as a relatively cleaner energy source, finds wide applications in urban gas supply, industrial manufacturing and power generation. The marine transportation of

*Corresponding author.

Email addresses: chenxi.zhao@tum.de (Chenxi Zhao), derek.wu1026@163.com (Yan Wu), yongchuan.yu@tum.de (Yongchuan Yu), oskar.haidn@tum.de (Oskar J. Haidn), xiangyu.hu@tum.de (Xiangyu Hu)

LNG has always been a topic of paramount importance. Due to the complicated and changeable conditions at the seas, the sloshing behaviours of the liquid in LNG tanks with the effects of wind and waves deserve attention. Several experiments have been conducted to replicate sloshing phenomena in horizontal tanks under external excitation [1, 2], and the application of baffles was demonstrated to exert effective influences on mitigating the liquid sloshing [3, 4, 5, 6].

On the other hand, the experimental work is usually constrained by its expenses in time and space, whereas the theoretical analyses are suitable for linear or weakly nonlinear sloshing problems [7, 8, 9, 3]. The advent of numerical simulation technology has expanded the toolkit for dealing with highly nonlinear sloshing motions. Extensive numerical investigations have been carried out regarding the interaction between tank sloshing and various types of baffles. In the aspect of grid-based methods, Cho et al. [10] and Biswal et al. [11] studied the rigid baffles in two-dimensional tanks with the finite element method (FEM), and improved the free-surface tracking technique. Many researchers have utilized the finite difference method (FDM) [12, 13, 14, 15, 16] or the finite volume method (FVM) [17, 18, 19] to solve Navier-Stokes equations of fluid dynamics in tanks. Tang et al. [20] compared the effect of different height allocation schemes of vertical baffles with the $k-\epsilon$ model, which indicated that the unequal baffle height has greater potential for sloshing suppression. Xue et al. [21] conducted numerical investigations on the seiche oscillations of layered fluids, and their findings suggested that the vertical baffles accelerate the wave decay and also affect the dominant response frequencies. As for meshless methods, Hwang et al. [22] employed a modified moving particle simulation approach to simulate the sloshing flows in partially filled tanks with elastic baffles. Aly et al. [7] established an incompressible SPH method with the Neumann pressure boundary to improve the calculation accuracy of highly nonlinear sloshing problems in long-time simulation, and performed this method on liquid sloshing with floating and middle baffles. Cao et al. [23] adopted the SPH method and found that when the ratio of the height of the baffle to that of the still liquid is over 0.5, it leads to an increase in the lowest natural frequency to reduce liquid sloshing. Additionally, simulations have explored tanks equipped with other types of baffles, such as porous baffles [24, 25], T-shaped baffles [16, 26, 27] and orifice baffles [28].

Violent oscillations can impose significant pressure loads on tanks, leading to structural instability or even failure. It is therefore crucial to figure out the hydrodynamic forces exerted by the fluid onto the walls. Lee et al. [29] numerically studied the sensitivity of a series of parameters to the impact pressure on LNG tanks to point out the compressibility of ullage spaces as an essential

parameter. A simple formula was derived by Chen et al.[13] to calculate the horizontal force coefficient C_f on the tank walls, indicating that at high excitation frequencies, C_f is dominated by mass effects, otherwise by the free-surface displacement. Besides, Delorme et al. [30] introduced an SPH formulation capable of simulating breaking waves impacting on tank walls, whereas the SPH results tended to overestimate the pressure maxima and impulse compared to experimental data. This may be caused by not considering the air phase in the numerical process. In addition, a considerable amount of work has demonstrated that the baffles significantly reduce the sloshing pressure acting on the walls on the basis of experiment and simulation results [12, 22, 31, 27]. An experiment was carried out by Akyildiz and Unal [32] to study the non-linear behaviour and damping characteristics of liquid sloshing in the tank with/without baffles. Different fill depths and excitations were imposed on the sloshing model to investigate the pressure distributions and three-dimensional effects on sloshing loads.

The displacement of the free surface stands as a crucial element when evaluating the sloshing intensity, and its tracking is consistently a fundamental challenge within tank sloshing simulations. Various computational methods in the Eulerian approach such as volume-of-fluid (VOF) [13, 25, 24] and level-set [33] were introduced to address the discontinuity of liquid motion or breaking waves problems, which are often encountered in conventional grid-based methods. However, it is still a great challenge for them to handle large deformations of the fluid [7]. In comparison, the boundary capture in both Lagrangian and arbitrary Lagrangian-Eulerian (ALE) approaches is more straightforward because the mesh precisely moves with fluid particles. As a meshless method, SPH offers remarkable benefits in addressing large deformations, free surfaces and moving boundaries due to its inherent self-adaptive and Lagrangian characteristics [34, 35]. SPH has already been utilized in free-surface tracking in liquid sloshing problems by some researchers [36, 23, 37, 38]. Solving governing equations with a single-phase model in SPH can lead to overestimated pressure [30, 39] as mentioned earlier, whereas the accuracy of impact pressure simulations near the tank corners was confirmed to be enhanced in terms of mean and peak pressures by introducing the air phase to SPH simulation [40]. Yet now to the best of our knowledge, there is a scarcity of computational solutions addressing the deformable structures of tanks. Even though the force of fluid on the walls has been calculated in the published work, the detailed stress and strain distribution of the solid walls cannot be obtained from the numerical models employing rigid bodies. Therefore, it is in great demand for precise modelling of the interaction between the two-phase flow and the tank

walls.

For the fluid-structure interaction problems, combining a single fluid solver with a single solid solver is commonly applied. FEM, as the most conventional methodology for solid mechanics, is often applied to treat structural deformations in FSI problems. In the previous experience in sloshing simulations, it has been coupled with grid-based methods such as FDM [41, 15] and FVM, or meshless methods such as moving particle semi-implicit (MPS) [42] and SPH [43]. Zhang et al. [44, 37] proposed a coupling strategy involving the smoothed finite element method (SFEM) and an improved SPH to investigate sloshing mitigation using elastic baffles. In this strategy, SFEM excels in addressing the "overly-stiff" problem compared to the conventional FEM. Additionally, several computational efforts referring to liquid sloshing problems only rely on particle-based FSI solvers. Hwang [22] et al. presented a modified MPS-based FSI solver with the incorporation of a free-surface assessment scheme in the fluid model to enhance its performance. Hu et al. [45] simulated the water in a rectangular tank interacting with an elastic baffle through the SPH-SPIM coupled method. However, the use of multiple solvers in a simulation can result in time-consuming, data loss or interpolation errors in the process of data transfer.

The objective of this work is to simulate the fluid flow regimes as well as the structural mechanics of walls during the sloshing procedure of LNG tanks, and to find out the damping mechanism of baffles on sloshing. Aiming at the above problems, we employ a multi-physics solver called SPHinXsys [46], which operates within a single framework. In this work, we first simulate both the fluid and solid domains using the SPH method. This approach avoids the excessive mesh distortion of fluid elements near the free-surface region in the grid-based methods, and also reduces the errors while transferring physical information between the fluid and solid domains. Second, the multi-phase model in terms of the water and air phases is conducted to be close to the actual utilization scenario of the LNG tanks. Third, the walls of the tanks are considered to be elastic to acquire the stress and strain distributions. All simulations are carried out in three dimensions to represent the actual physical fields better. The framework of this work is as follows: Section 2 introduces the numerical methods in this work. Section 3 provides the verification process to assess the reliability of the numerical simulation tool; Section 4 discusses the influence of ring baffles and vertical baffles on liquid sloshing degree and force exerted on tanks and Section 5 compares the different effects of rigid and elastic baffles on sloshing suppression. Finally, some conclusions are drawn in Section 6.

2. Methodology

2.1. Fluid dynamics method based on a multi-phase Riemann solver

In this work, a multi-phase model consisting of two viscous and immiscible fluids with a high density ratio is adopted. The mass and momentum conservation equations can be expressed respectively as

$$\frac{d\rho}{dt} = -\rho \nabla \cdot \mathbf{v} \quad (1)$$

$$\frac{d\mathbf{v}}{dt} = \frac{1}{\rho} (-\nabla p + \eta \nabla^2 \mathbf{v}) + \mathbf{f}^{s:p} + \mathbf{f}^{s:\nu} + \mathbf{f}^e \quad (2)$$

where d/dt is the material derivative, and ρ , \mathbf{v} , p , η denote the density, the velocity, the pressure and the dynamic viscosity respectively. The force exerted on the fluid by the wall boundary is divided into pressure force $\mathbf{f}^{s:p}$ and viscous force $\mathbf{f}^{s:\nu}$. Besides, an external force \mathbf{f}^e is added to the fluid.

The weakly compressible SPH (WCSPH) method is the most widely used method for incompressible multi-phase flows, while it may produce spurious pressure oscillation problems [47]. Aiming at the violent water-air flow cases in this work, the modified form of WCSPH in Ref.[48] has been conducted. The modification refers to the low-dissipation Riemann solver and the application of transport-velocity formulation in the light phase. The fluid pressure is calculated by density from an artificial equation of state:

$$p = c^2(\rho - \rho_0) \quad (3)$$

where c represents the numerical speed of sound and is defined as $c = 10V_{\max}$. The speed of sound of the heavy and light phases are the same. V_{\max} is evaluated by $V_{\max} = 2\sqrt{gh_w}$, meaning the maximum anticipated flow speed. g is the gravitational acceleration, h_w is the depth of water and ρ_0 is the reference density of the fluid.

In the WCSPH based on a multi-phase Riemann solver, the heavy phase is regarded as the moving boundary for the light phase, while itself is considered as a free-surface-like flow with variable free-surface pressure [49]. The SPH discretization of continuity and momentum equations can be written as:

$$\frac{d\rho_i}{dt} = 2\rho_i \sum_j \frac{m_j}{\rho_j} (\mathbf{v}_i - \mathbf{v}^*) \cdot \nabla_i W_{ij} \quad (4)$$

$$\frac{d\mathbf{v}_i}{dt} = -2 \sum_j m_j \frac{p^*}{\rho_i \rho_j} \nabla_i W_{ij} + 2 \sum_j m_j \frac{\eta_{ij}}{\rho_i \rho_j} \frac{\mathbf{v}_{ij}}{r_{ij}} \frac{\partial W_{ij}}{\partial r_{ij}} + \mathbf{f}_i^{s:p} + \mathbf{f}_i^{s:\nu} + \mathbf{f}_i^e \quad (5)$$

Here, m_j is the particle mass, $\mathbf{v}_{ij} = \mathbf{v}_i - \mathbf{v}_j$ and $\eta_{ij} = \frac{2\eta_i \eta_j}{\eta_i + \eta_j}$. The gradient of kernel function $\nabla_i W_{ij} = \mathbf{e}_{ij} \frac{\partial W_{ij}}{\partial r_{ij}}$ with $\mathbf{e}_{ij} = -\mathbf{r}_{ij}/r_{ij}$ representing the unit vector from particle i to j . \mathbf{v}^* and p^* denote the solutions of an inter-particle Riemann problem along \mathbf{e}_{ij} . The construction along the interface between particle i and particle j as well as the structure of the solution are shown in Fig.1, with the initial left and right states reconstructed as

$$\begin{cases} (\rho_L, U_L, p_L) = (\rho_i, \mathbf{v}_i \cdot \mathbf{e}_{ij}, p_i) \\ (\rho_R, U_R, p_R) = (\rho_j, \mathbf{v}_j \cdot \mathbf{e}_{ij}, p_j) \end{cases} \quad (6)$$

where subscripts L and R represent the left and right states of the one-dimensional Riemann problem. The middle wave is always a contact discontinuity separating two intermediate states, i.e. (ρ_L^*, U_L^*, p_L^*) and (ρ_R^*, U_R^*, p_R^*) . An assumption $U^* = U_L^* = U_R^*$ and $p^* = p_L^* = p_R^*$ is adopted at the intermediate state, and then the intermediate velocity and pressure can be approximated by

$$\begin{cases} U^* = \bar{U} + \frac{p_L - p_R}{c(\rho_L + \rho_R)} \\ p^* = \bar{p} + \frac{\rho_L \rho_R \beta (U_L - U_R)}{\rho_L + \rho_R} \end{cases} \quad (7)$$

Here, $\bar{U} = (\rho_L U_L + \rho_R U_R)/(\rho_L + \rho_R)$ and $\bar{p} = (\rho_L p_R + \rho_R p_L)/(\rho_L + \rho_R)$. The dissipation limiter $\beta = \min(3\max(U_L - U_R, 0), c)$ proposed in ref[50] is introduced for p^* to reduce the numerical dissipation. Then \mathbf{v}^* in Eq.(2) is derived by $\mathbf{v}^* = U^* \mathbf{e}_{ij} + (\bar{\mathbf{v}}_{ij} - \bar{U} \mathbf{e}_{ij})$, and $\bar{\mathbf{v}}_{ij} = (\rho_i \mathbf{v}_i + \rho_j \mathbf{v}_j)/(\rho_i + \rho_j)$.

Additionally, in fluid dynamics simulations, the tensile instability in the WCSPH method results in particle clumping and unnatural void regions when negative pressure occurs. Hence, the transport-velocity formulation presented by Adami et al. [51] and Zhang et al. [52] is applied to the light phase to avoid this issue. However, the heavy phase does not need it because the pressure distribution is always positive as a consequence of gravity. The particle advection velocity $\tilde{\mathbf{v}}$ is obtained by employing a background pressure p_b at every time step:

$$\tilde{\mathbf{v}}_i(t + \delta t) = \mathbf{v}_i(t) + \delta t \left(\frac{d\mathbf{v}_i}{dt} - 2p_b \sum_j m_j \frac{1}{\rho_i \rho_j} \nabla_i W_{ij} \right) \quad (8)$$

With the transport velocity, the momentum equation of Eq.5 can be rewritten as

$$\frac{d\mathbf{v}_i}{dt} = -2 \sum_j m_j \frac{p^*}{\rho_i \rho_j} \nabla_i W_{ij} + 2 \sum_j m_j \frac{\eta_{ij}}{\rho_i \rho_j} \frac{\mathbf{v}_{ij}}{r_{ij}} \frac{\partial W_{ij}}{\partial r_{ij}} + 2 \sum_j m_j \frac{\bar{\mathbf{A}}_{ij}}{\rho_i \rho_j} \nabla_i W_{ij} + \mathbf{g}_i + \mathbf{f}_i^{s:p} + \mathbf{f}_i^{s:\nu} + \mathbf{f}_i^e \quad (9)$$

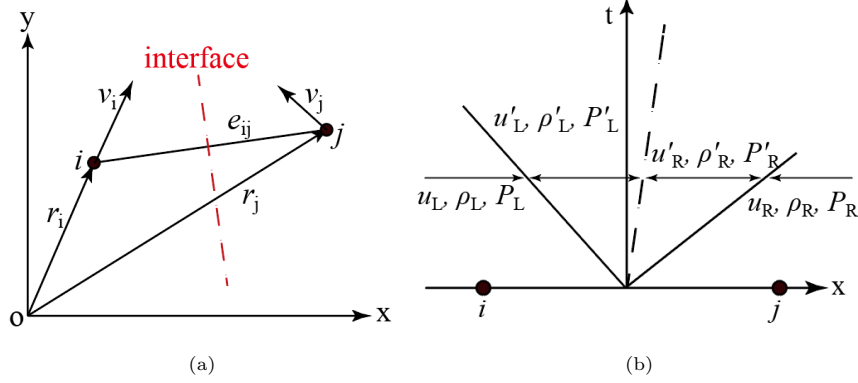


Figure 1: WCsPH method based on a Riemann solver [50]: (a) Construction of Riemann problem along the interacting line of particles i and j , (b) Simplified Riemann fan with two intermediate states.

where $\bar{\mathbf{A}}_{ij} = (\mathbf{A}_i + \mathbf{A}_j)/2$. $\mathbf{A}_i = \rho_i \mathbf{v}_i (\tilde{\mathbf{v}}_i - \mathbf{v}_i)$ means an extra stress tensor due to the advection velocity $\tilde{\mathbf{v}}$. Specifically, $\tilde{\mathbf{v}}$ equals to \mathbf{v}_j for the heavy phase.

In SPHinXsys, dummy particles are adopted to impose the solid wall boundary [53]. The interaction between the fluid particles and wall dummy particles is determined by the one-sided Riemann problem as shown in Fig.2 with the following intermediate pressure [54]:

$$p^* = \frac{\rho_f p_w + \rho_w p_f}{\rho_f + \rho_w} \quad (10)$$

where subscripts f and w represent the fluid and wall respectively. Also, U^* is still acquired by Eq.(7). The pressure of wall dummy particles is calculated by

$$p_w = \frac{\sum_f p_f W_{wf} + (\mathbf{g} - \mathbf{a}_w) \cdot \sum_f \rho_f \mathbf{r}_{wf} W_{wf}}{\sum_f W_{wf}} \quad (11)$$

where a_w is the acceleration of the wall. Particularly, the Eq.(11) is divided by ρ_f to remove the contribution of heavy phase particles in p_w at a triple point, i.e. light phase, heavy phase and solid wall.

Besides, for the physical situations in the present study, penalty force is introduced to effectively prevent particle penetration in violent impacts and multi-phase flows with a high density ratio [54]. When the particle of the light phase is close to the wall boundary, the penalty force can be calculated as

$$\mathbf{F}_p = -2 \sum_w \frac{m_w}{\rho_i \rho_w} \Gamma(\mathbf{r}_i, \mathbf{r}_w) \mathbf{n}_w \frac{1}{|\mathbf{r}_{iw}|^2} \frac{\partial W_{iw}}{\partial(|\mathbf{r}_{iw}|)} \quad (12)$$

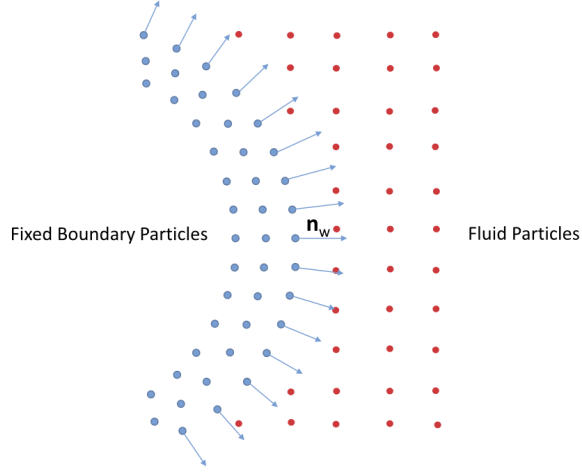


Figure 2: Sketch of fluid particles interacting with fixed wall boundary particles along the wall-normal direction through the one-side Riemann problem [50].

Here subscripts i and w denote the light phase particles and wall particles, and n_w is the predicted unit normal vector of the wall particles. $\Gamma(\mathbf{r}_i, \mathbf{r}_w)$ is the penalty parameter evaluated by

$$\Gamma(\mathbf{r}_i, \mathbf{r}_w) = \gamma_p |p_i \mathbf{e}_{iw} \cdot \mathbf{n}_w| \begin{cases} \frac{(1 - \delta)^2}{\Delta x}, & \delta < 1 \\ 0, & \delta \geq 1 \end{cases} \quad (13)$$

where Δx is the initial particle spacing and $\delta = 2|\mathbf{r}_{iw}|(\mathbf{e}_{iw} \cdot \mathbf{n}_w)/\Delta x$.

To further enhance the robustness and accuracy of the simulation approach, a reinitialization method referring to the density field is introduced in Ref.[54], which can be expressed as the following equations for the free-surface-like flow of the water as well as the air with the moving boundary respectively.

$$\rho_i = \rho^0 \frac{\sum W_{ij}}{\sum W_{ij}^0} + \max(0, \rho^* - \rho^0 \frac{\sum W_{ij}}{\sum W_{ij}^0}) \frac{\rho^0}{\rho^*} \quad (14)$$

$$\rho_i = \rho^0 \frac{\sum W_{ij}}{\sum W_{ij}^0} \quad (15)$$

where ρ^* stands for the density before reinitialization and the subscript 0 means the initial state.

2.2. Solid Dynamics

The deformation tensor \mathbb{F} can be derived from the displacement $\mathbf{u} = \mathbf{r} - \mathbf{r}^0$ by

$$\mathbb{F} = \nabla^0 \mathbf{u} + \mathbf{I} \quad (16)$$

The mass and momentum conservation equations of solid mechanics in a Lagrangian framework are established as

$$\rho = \rho_0 \frac{1}{J} \quad (17)$$

$$\frac{d\mathbf{v}}{dt} = \frac{1}{\rho^0} \nabla^0 \cdot \mathbb{P}^T + \mathbf{f}^{f:p} + \mathbf{f}^{f:\nu} \quad (18)$$

where $J = \det(\mathbb{F})$ is the Jacobian determinant of deformation tensor \mathbb{F} , $\mathbb{P} = \mathbb{F}\mathbb{S}$ is the first Piola-Kirchhoff stress tensor with \mathbb{S} denoting the second Piola-Kirchhoff stress tensor, which can be simplified by Eq.(19) when the material is linearly elastic and isotropic. $\mathbf{f}^{f:p}$ and $\mathbf{f}^{f:\nu}$ represent the pressure and viscous forces from the fluid on the solid.

$$\begin{aligned} \mathbb{S} &= K \text{tr}(\mathbb{E}) \mathbf{I} + 2G \left(\mathbb{E} - \frac{1}{3} \text{tr}(\mathbb{E}) \mathbf{I} \right) \\ &= \lambda \text{tr}(\mathbb{E}) \mathbf{I} + 2\mu \mathbb{E} \end{aligned} \quad (19)$$

where $K = \lambda + (2\mu/3)$ and $G = \mu$ represent the bulk modulus and shear modulus respectively. λ and μ are the Lamé parameters. Note that the bulk and shear modulus can be expressed by the Young's modulus E and Poisson's ratio ν as Eq.(20). The Green-Lagrange strain tensor \mathbb{E} is described based on the deformation tensor \mathbb{F} by Eq.(21).

$$E = 2G(1 + 2\nu) = 3K(1 - 2\nu) \quad (20)$$

$$\mathbb{E} = \frac{1}{2} (\mathbb{F}^T \mathbb{F} - \mathbf{I}) \quad (21)$$

SPHinXsys adopts the total Lagrangian formulation for solid mechanics. The initial reference configuration is applied to search the neighboring particles and the set of neighboring particles is not updated. The mass and momentum conservation equation for solid particles are discretized as

$$\rho_i = \rho^0 \frac{1}{\det(\mathbb{F})} \quad (22)$$

$$\frac{d\mathbf{v}_a}{dt} = \sum_b \frac{m_b}{\rho_a \rho_b} (\mathbb{P}_a \mathbb{B}_a^0 + \mathbb{P}_b \mathbb{B}_b^0) \nabla_a^0 W_{ab} + \mathbf{f}_a^{s:p} + \mathbf{f}_a^{s:\nu} \quad (23)$$

where the subscript a means the solid particle. The correction matrix $\mathbb{B}_a^0 = (\sum_b \frac{m_b}{\rho_b} (\mathbf{r}_b^0 - \mathbf{r}_a^0) \otimes \nabla_a^0 W_{ab})^{-1}$ is introduced to ensure the homogeneity and isotropy of space in the process of spatial discretization [55]. The deformation tensor \mathbb{F} is calculated as

$$\mathbb{F} = \left(\sum_b \frac{m_b}{\rho_b} (\mathbf{u}_b - \mathbf{u}_a) \otimes \nabla_a^0 W_{ab} \right) \mathbb{B}_a^0 + \mathbf{I} \quad (24)$$

2.3. Fluid-Structure Interaction

As mentioned in the introduction section, the fluid-structure interaction among water, air and wall will be conducted in this paper. SPHinXsys benefits from its multi-resolution framework, namely that the fluid and solid domains in FSI problems can be discretized by different spatial-temporal resolutions [56]. The smoothing length for fluid and solid discretization are expressed as h_f and h_s , and $h_f \geq h_s$. In this work, $h_f = 1.3\Delta x$ and $h_s = 1.15\Delta x$. Detailedly, the pressure force and viscous force exerted on fluid by solid in Eq.(9) are described as

$$\mathbf{f}_i^{s:p}(h_f) = -2 \sum_a m_a \frac{p^*}{\rho_i \rho_a} \nabla_i W(\mathbf{r}_{ia}, h_f) \quad (25)$$

$$\mathbf{f}_i^{s:\nu}(h_f) = 2 \sum_a m_a \frac{\eta_{ia}}{\rho_i \rho_a} \frac{\mathbf{v}_i - \mathbf{v}_a^d}{|\mathbf{r}_{ia}| + 0.01h} \frac{\partial W(\mathbf{r}_{ia}, h_f)}{\partial r_{ia}} \quad (26)$$

Here, $p^* = (p_i \rho_a^d + p_a^d \rho_i) / (\rho_i + \rho_a^d)$ is the Riemann solution of the one-sided Riemann problem whose left and right states are given as Eq.(27). \mathbf{v}_d is the imaginary velocity of the solid particle.

$$\begin{cases} (\rho_L, U_L, p_L) = (\rho_i, -\mathbf{v}_i \cdot \mathbf{n}_a, p_i) \\ (\rho_R, U_R, p_R) = (\rho_a, -\mathbf{v}_a^d \cdot \mathbf{n}_a, p_a^d) \end{cases} \quad (27)$$

where \mathbf{n}_a means the local normal vector from solid particle to fluid particle. The forces acting on the solid by fluid are described as

$$\begin{cases} \mathbf{f}^{f:p} = -\mathbf{f}^{s:p} \\ \mathbf{f}^{f:\nu} = -\mathbf{f}^{s:\nu}. \end{cases} \quad (28)$$

2.4. Sloshing Making

In the present work, pitching excitation is considered to simulate the liquid sloshing in the tank. The tank is assumed to be fixed and the reverse external force is applied to the multi-phase flow. According to Xue and Lin [14], the external acceleration \mathbf{f}^e of the momentum equation in Eq.(2) for both water and air phases are expressed as

$$\mathbf{f} = \mathbf{g} - \frac{d\mathbf{U}}{dt} - \frac{d\mathbf{\Omega}}{dt} \times (\mathbf{r} - \mathbf{R}) - 2\mathbf{\Omega} \times \frac{d(\mathbf{r} - \mathbf{R})}{dt} - \mathbf{\Omega} \times [\mathbf{\Omega} \times (\mathbf{r} - \mathbf{R})] \quad (29)$$

where \mathbf{U} and $\mathbf{\Omega}$ are the translational and rotational velocities of non-inertial coordinate respectively. \mathbf{R} and \mathbf{r} are the original point of rotational motion and the local position vector.

Specifically, to prevent the tank from running away under the force of liquid when the walls of the tank are replaced with elastic material, the constraints composed of translation and rotation are proposed for fixing the tank. The total momentum of the tank \mathbf{P} is calculated through

$$\mathbf{P} = \sum_a m_a \cdot \mathbf{v}_a \quad (30)$$

Subsequently, the translational velocity of the tank $\bar{\mathbf{v}}_{\text{tank}}$ is computed through the equation $\bar{\mathbf{v}}_{\text{tank}} = \mathbf{P}/m_{\text{total}}$ with the total mass of tank m_{total} . Further, the velocity of each tank particle should be subtracted from the translational velocity. Once the tank's translational movement is confined, the rotational motion will conduct around its center of mass. The angular momentum of the tank \mathbf{L} is written as

$$\mathbf{L} = \mathbf{r} \times (m\mathbf{v}) = \mathbb{I}\omega \quad (31)$$

Therefore, the angular velocity of the tank ω equals to $\mathbb{I}^{-1} \times \mathbf{L}$, where \mathbb{I} signifies the inertia tensor. Then the velocity of each tank particle should be adjusted by subtracting the linear velocity of the tank, i.e. $\mathbf{v}_{\text{tank}}^{\text{linear}} = \omega \times \mathbf{r}$.

2.5. Artificial-viscosity-based damping method

To initiate sloshing while the water is relatively still, only downward gravitational acceleration is applied to the fluid during the initial second. Moreover, an extra artificial-viscosity-based damping term, as described in Ref.[57], is introduced into the momentum equation at this stage to effectively dissipate velocity gradients while preserving the system's momentum conservation. The local damping term in implicit format can be written as

$$\mathbf{f}_i^\nu = 2\eta \sum_j \frac{m_j}{\rho_i \rho_j} \frac{\mathbf{v}_{ij}^{n+1}}{\mathbf{r}_{ij}} \frac{\partial W_{ij}}{\partial r_{ij}} \quad (32)$$

where $\mathbf{v}_{ij}^{n+1} = \mathbf{v}_{ij}^n + d\mathbf{v}_i - d\mathbf{v}_j$ with $d\mathbf{v}_i$ and $d\mathbf{v}_j$ denoting the incremental velocity change of particle i and its neighboring particles j (including both internal and contact configurations of the particle i) induced by viscous acceleration.

Further, here we employ the pairwise splitting scheme proposed by Zhu[57] for an implicit velocity update, from which $d\mathbf{v}_i$ and $d\mathbf{v}_j$ can be derived as follows:

$$\begin{cases} d\mathbf{v}_i = m_j \frac{B_j \mathbf{v}_{ij}}{m_i m_j - (m_i + m_j) B_j} \\ d\mathbf{v}_j = -m_i \frac{B_j \mathbf{v}_{ij}}{m_i m_j - (m_i + m_j) B_j} \end{cases} \quad (33)$$

where B_j is defined as

$$B_j = 2\eta \frac{m_j}{\rho_i \rho_j} \frac{1}{\mathbf{r}_{ij}} \frac{\partial W_{ij}}{\partial \mathbf{r}_{ij}} dt. \quad (34)$$

2.6. Time Steps

The time step size of fluid and solid simulation are limited by the CFL condition for numerical stability. The dual-criteria time stepping for fluid dynamics is employed in SPHinXsys, which is characterized by particle advection and acoustic speeds [58]. More precisely, the time-step size determined by the advection criterion, symbolized as Δt_{ad} , and that determined by the acoustic criterion, symbolized as Δt_{ac} , are defined through Eq.(35) and Eq.(36). The advection criterion controls the update of the neighbor particle list and the corresponding kernel weights and gradients, while the acoustic criterion determines the time integration of the particle density, position and velocity.

$$\Delta t_{ad} = CFL_{ad} \min\left(\frac{h}{|\mathbf{v}|_{\max}}, \frac{h^2}{\nu}\right) \quad (35)$$

$$\Delta t_{ac} = CFL_{ac} \frac{h}{c + |\mathbf{v}|_{\max}} \quad (36)$$

where $CFL_{ad} = 0.25$ and $CFL_{ac} = 0.6|\mathbf{v}|_{\max}$ and ν mean the maximum particle advection speed and kinematic viscosity respectively.

For the time integration of solid equations, the time-step criterion Δt^s is defined as

$$\Delta t^s = 0.6 \min\left(\frac{h^s}{c^s + |\mathbf{v}|_{\max}}, \sqrt{\frac{h^s}{\left|\frac{d\mathbf{v}}{dt}\right|_{\max}}}\right) \quad (37)$$

Further, the structure time stepping is coupled with the dual-criteria time stepping for the FSI problem. In SPHinXsys, the position-based Verlet scheme is employed, that is in one advection time step Δt_{ad} , the acoustic time step Δt_{ac} is repeated for the pressure relaxation process until the accumulated time interval exceeds Δt_{ad} . At the beginning of every advection time step, the density field is reinitialized by Eq.(14) and Eq.(15) for heavy and light phases respectively. The first half-step velocity in the n acoustic time step is updated as

$$\mathbf{v}_i^{n+\frac{1}{2}} = \mathbf{v}_i^n + \frac{\Delta t_{ac}}{2} \left(\frac{d\mathbf{v}_i}{dt}\right)^n \quad (38)$$

Then the updated velocity at the midpoint is applied to obtain the particle position and density in the meantime for the next acoustic time step

$$\mathbf{r}_i^{n+1} = \mathbf{r}_i^n + \Delta t_{ac} \mathbf{v}_i^{n+\frac{1}{2}} \quad (39)$$

$$\rho_i^{n+1} = \rho_i^n + \frac{\Delta t_{ac}}{2} \left(\frac{d\rho_i}{dt} \right)^{n+\frac{1}{2}} \quad (40)$$

At last, the velocity of the particle i at the end of this acoustic time step is obtained by

$$\mathbf{v}_i^{n+1} = \mathbf{v}_i^n + \frac{\Delta t_{ac}}{2} \left(\frac{d\mathbf{v}_i}{dt} \right)^{n+1} \quad (41)$$

For the time integration of solid equations, generally $\Delta t^s < \Delta t_{ac}$. Index $x = 0, 1, \dots, k-1$ is utilized within one acoustic time step of fluid integration with $k = \lceil \frac{\Delta t_{ac}}{\Delta t^s} \rceil + 1$. The deformation tensor, density and particle position are updated to the midpoint as

$$\mathbb{F}_a^{x+\frac{1}{2}} = \mathbb{F}_a^x + \frac{\Delta t^s}{2} \frac{d\mathbb{F}_a}{dt} \quad (42)$$

$$\rho_a^{x+\frac{1}{2}} = \rho_a^0 \frac{1}{J} \quad (43)$$

$$\mathbf{r}_a^{x+\frac{1}{2}} = \mathbf{r}_a^x + \frac{\Delta t^s}{2} \mathbf{v}_a^x \quad (44)$$

After that, the velocity of solid particle a is updated to the next time step

$$\mathbf{v}_a^{x+1} = \mathbf{v}_a^x + \Delta t^s \frac{d\mathbf{v}_a}{dt} \quad (45)$$

Finally, the deformation tensor and position of solid particles are updated to the new time step by

$$\mathbb{F}_a^{x+1} = \mathbb{F}_a^{x+\frac{1}{2}} + \frac{\Delta t^s}{2} \frac{d\mathbb{F}_a}{dt} \quad (46)$$

$$\rho_a^{x+1} = \rho_a^0 \frac{1}{J} \quad (47)$$

$$\mathbf{r}_a^{x+1} = \mathbf{r}_a^{x+\frac{1}{2}} + \frac{\Delta t^s}{2} \mathbf{v}_a^{x+1} \quad (48)$$

2.7. Algorithm

The simulation procedure of the multi-phase liquid sloshing in an elastic tank is shown in Algorithm 1.

Algorithm 1: Multi-phase liquid sloshing in an elastic tank

```
1 Setup geometrical and material parameters;
2 Generate particle distribution;
3 while simulation termination condition is not satisfied do
4   Calculate  $\Delta t_{ad}$  for water and air;
5    $Dt = \min(\Delta t_{ad}^w, \Delta t_{ad}^a)$ ;
6   Reinitialize density with Eq.(14) for water and Eq.(15) for air;
7   Calculate transport velocity for air with Eq.(9);
8   Calculate viscous force on fluid particles with viscosity term in Eq.(26);
9   Calculate viscous force on the tank wall with Eq.(26 and Eq.(28);
10  Update wall normal vector;
11  while relaxation time < Dt do
12    Calculate  $\Delta t_{ac}$  for water and air;
13     $dt = \min(\Delta t_{ac}^w, \Delta t_{ac}^a, Dt)$ ;
14    while physical time < 1 second do
15      Execute fluid damping process with Eq.(32);
16    end
17    Update the velocity of fluid particles to the midpoint with Eq.(38);
18    Update the pressure force on fluid particles with Eq.(25);
19    Update the pressure force on the tank wall with Eq.(28);
20    Update the position and density of fluid particles with Eq.(39) and Eq.(40) respectively;
21    Update the velocity of fluid particles to next time step with Eq.(41);
22    while  $dt_{sum}^s < dt$  do
23      Calculate  $\Delta t^s$  for solid;
24       $dt^s = \min(\Delta t^s, dt - dt_{sum}^s)$ ;
25      Update  $\mathbb{F}$ ,  $\rho$  and  $\mathbf{r}$  of solid particles to the midpoint with Eq.(42), Eq.(43) and Eq.(44);
26      Update the velocity of solid particles with Eq.(45);
27      Constrain the elastic tank;
28      Update  $\mathbb{F}$ ,  $\rho$  and  $\mathbf{r}$  of solid particles to the next time step with Eq.(46), Eq.(47) and Eq.(48);
29    end
30    Update neighbor particle list, kernel values and gradient;
31    State Update particle configuration;
32  end
33 end
34 Terminate the simulation.
```

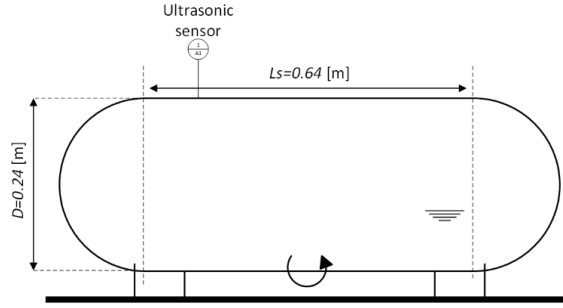


Figure 3: Experimental test setup [1]

3. Validation Tests

3.1. Comparison with LNG tank experiment

The previous research that simplifies the tank as a rigid body is often insufficiently accurate. The complex interaction between the tank's motions and deformations substantially impacts the predicted accuracy of the strain and stress distribution of the walls and the flow characteristics of the fluid. In this case, the tank walls are modelled as elastic bodies to provide a more comprehensive and realistic simulation condition. The simulation results are compared with the experiment carried out by Grotle and Æsøy [1] to validate the prediction accuracy of SPHinXsys. The experimental setup is shown in Fig.3, featuring a cylindrical tank with semi-elliptical heads at a 2:1 ratio, and the thickness of the tank is modelled as 0.018 meters. In this test, the tank undergoes pitching motion excitation, with the roll axis positioned at the intersection of the tank bottom and the center plane. The tank's motion angle is given as $\theta(t) \approx A \sin(2\pi ft)$, where A is the constant amplitude equal to 3 degrees, f [Hz] is the frequency of the motion with the value of 0.5496 and t [s] represents the physical time. A sensor is located at 0.122m away from the left-hand beginning of the straight cylindrical section to detect the free-surface height. For the validation case, we adopt a ratio of 0.255 between the water depth and the inside diameter of the tank, denoted as h_w/D . Additionally, the densities of the water and air are 1000 kg/m^3 and 1.226 kg/m^3 respectively.

Fig.4 indicates the comparison of the free surface elevation predicted by SPHinXsys, three-dimensional RANS model based on interDyMFoam solver with OpenFOAM and experimental data provided in Ref.[1]. Initial particle spacing values $\Delta x = 0.0045$ and 0.006 m are tested for grid independence, noting that the lower resolution does not provide three layers of wall particles required

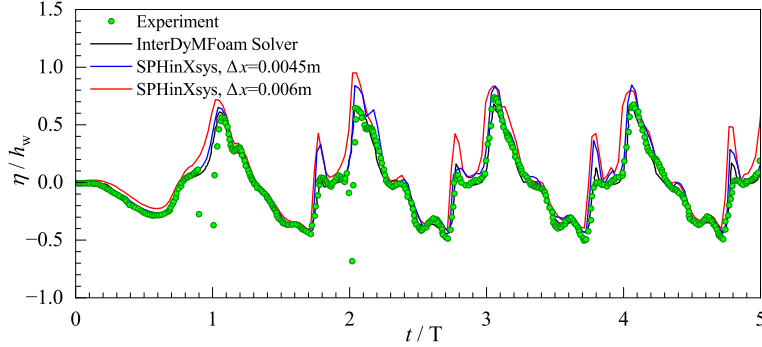


Figure 4: Comparison of non-dimensional free surface elevation of water between experiment [1] and simulations.

to achieve sufficient kernel support for fluid neighbors. The x-axis t/T stands for the ratio of physical time to the period of circular motion, while the y-axis η/h_w means the ratio of free surface elevation to the initial water depth. It is noted that the numerical sloshing wave elevation predicted by SPHinXsys closely follows the experimental trend, and its accuracy improves with increasing resolution. The pattern and period of wave heights obtained by SPH simulation are comparable with experimental observations. However, SPH tends to overestimate the amplitude, although it remains within an acceptable range. This higher amplitude estimation could be attributed to the influence of some splashing water particles on wave height estimation. To balance computational efficiency and numerical reliability, $\Delta x = 0.006$ m is chosen for the subsequent calculation.

Fig.5 presents the numerical and experimental free surface wave profiles when the wave travels back from the tank head. Fig.6 depicts the comparison of predicted wave profiles between interDyMFoam solver and SPHinXsys at several moments. Here the air domain is not displayed in SPH results for better visualization. At 16.20s, the wave reaches the frontal section of the tank, leading to the formation of a vertical fountain. The wave profile illustrated on the right-hand panels by SPH closely resembles that on the left-hand panels at the same time. Subsequently, as the wave retreats from the tank head, the vertical fountain dissipates. At this juncture, the wave profile obtained by SPH aligns remarkably well with the corresponding snapshot from the simulation conducted by the interDyMFoam solver. Following this, the wave maintains its propagation, prompting a rapid reduction in water depth near the wall. This observable phenomenon is captured in snapshots from both the SPHinXsys and interDyMFoam-solver-based simulations. Specifically, at 16.55s and 16.65s, the wave profiles simulated by SPHinXsys exhibit strong concordance with the results ob-

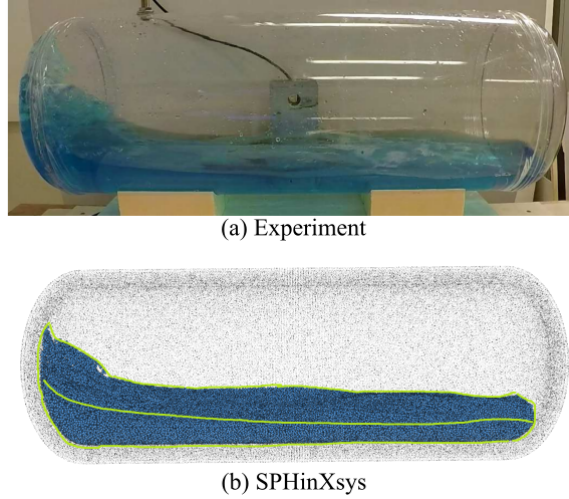


Figure 5: Wave profiles comparison between (a) experiment and (b) SPHinXsys.

tained through the `interDyMFoam` solver. The above analyses demonstrate that the SPHinXsys algorithm is effective in predicting liquid sloshing problems under pitching excitation.

3.2. Verification work before

Another robust validation is presented in the published literature by Ren et al. using SPHinXsys [38]. According to their work, the comparison between numerical results and experimental data or analysis solutions of liquid sloshing is performed, and satisfactory agreement can be obtained. This proves the reliability of SPHinXsys in evaluating parameters such as free surface elevation, pressure forces on baffles, and the displacement of elastic baffles. Therefore, the SPH method can be further used in the following work on free surface capture, force and deformation analysis referring to solid mechanics as well as the fluid-structure interaction process.

4. Analysis of fluid sloshing and force on the tank with/without baffles

This chapter involves the investigation of the force on the tank during the liquid sloshing process and the baffle effect on the suppression of sloshing behaviors. The density, Poisson ratio and Young's modulus of the tank are 7890 kg/m^3 , 0.27 and 135 GPa respectively. Note that the analysis begins with the sloshing behavior, i.e. the preloading process with the damping method is ignored.

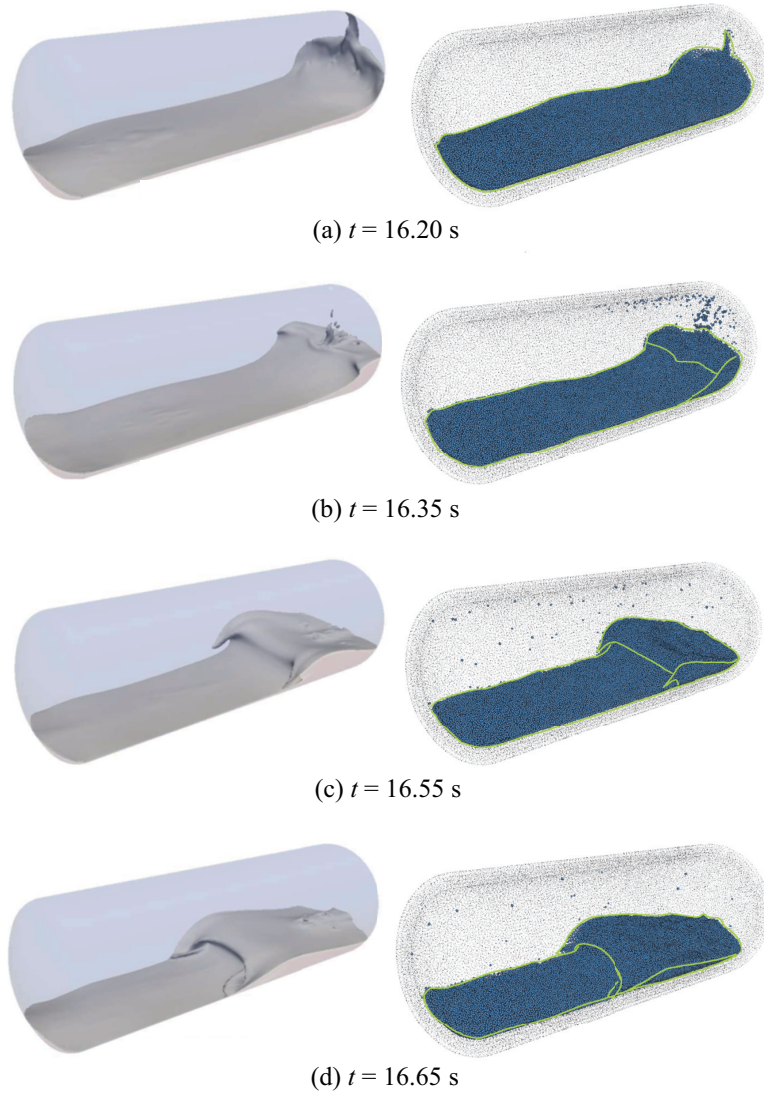


Figure 6: Wave profiles at different time: interDyMFoam-solver-based simulation (left-hand panels) [1] and SPHinXsys (right-hand panels).

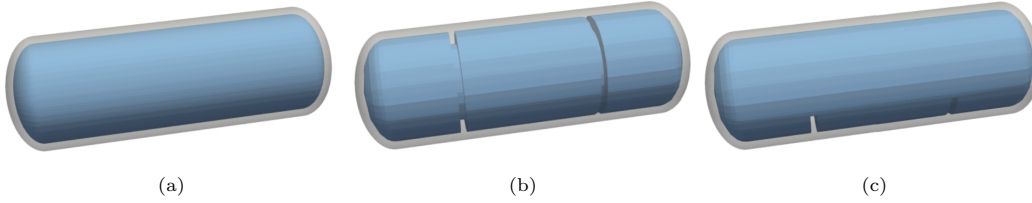


Figure 7: Structures of elastic tanks: (a) without baffle, (b) with 2 ring baffles and (c) with 2 vertical baffles.

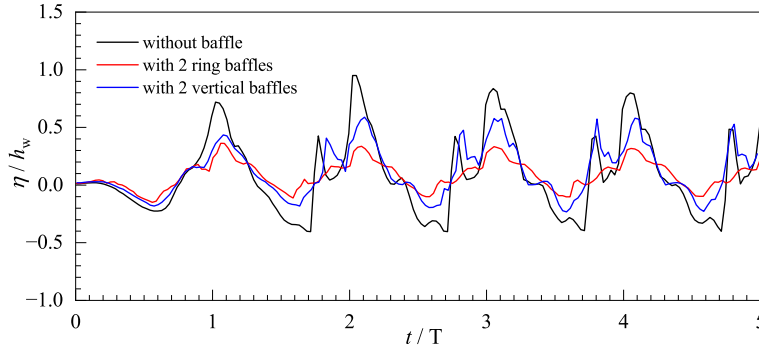


Figure 8: Comparison of non-dimensional free surface elevation of water among normal tank and tank with baffles

Fig.7 depicts the structures of the standard LNG tank as well as the tank equipped with two kinds of baffles: ring baffles and vertical baffles. Fig.8 presents a comparison of the non-dimensional free surface elevation of water among three tank configurations. The corresponding fluid regimes in the third period, when the sloshing becomes stable, are displayed in Fig.9, Fig.10 and Fig.11. Here, four representative moments are selected, including fluid preparing to swing to the right side, fluid hitting the right head of the tank and backflow after impact. Notably, the introduction of baffles facilitates mitigating sloshing effectively by disrupting wave propagation. In other words, the tanks incorporated two ring or vertical baffles alter the flow patterns of water and consequently affect the free surface height. Relatively speaking, ring baffles have a more pronounced effect on mitigating large oscillations in this numerical case.

The velocity of the primary wave occupies the maximum value, and the integration of baffles yields a noticeable refinement in the velocity distribution, resulting in a smoother pressure field and more controlled flow pattern. This improvement is instrumental in minimizing the turbulence and volatile motion that could otherwise affect the tanks' stability and structural integrity. Fig.11 exhibits the vorticity distribution during a series of sloshing events after water impacts the left

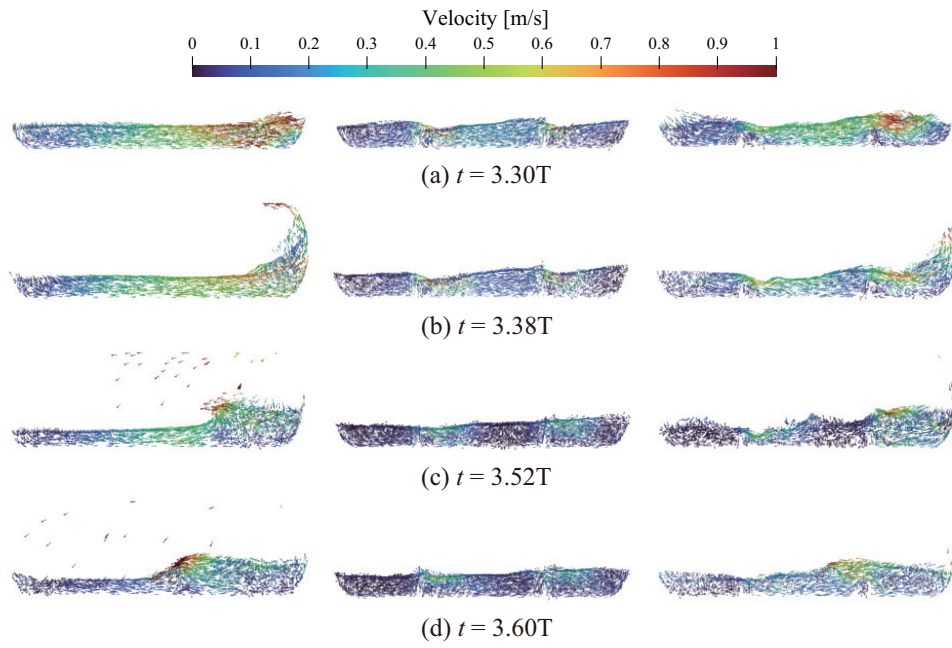


Figure 9: Velocity distributions of water in the third period. left: elastic tank without baffle, middle: elastic tank with 2 ring baffles, right: elastic tank with 2 vertical baffles.

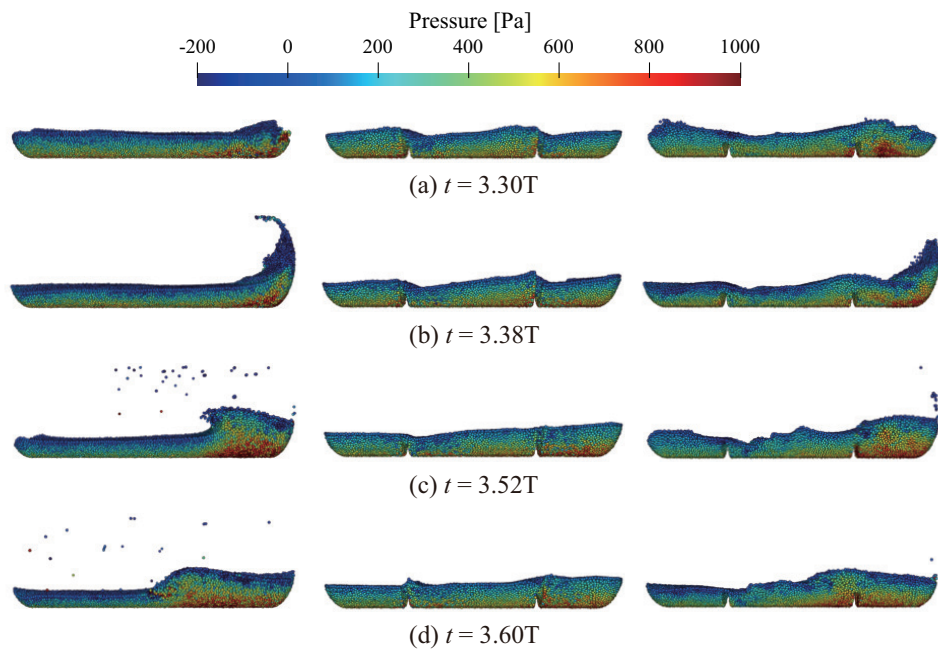


Figure 10: Pressure distributions of water in the third period. left: elastic tank without baffle, middle: elastic tank with 2 ring baffles, right: elastic tank with 2 vertical baffles.

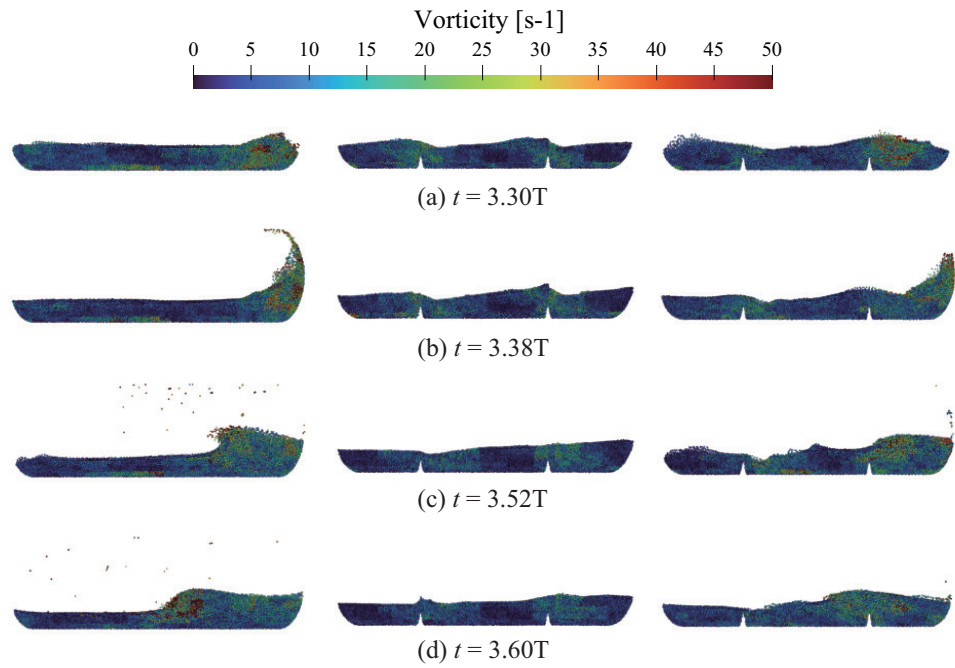


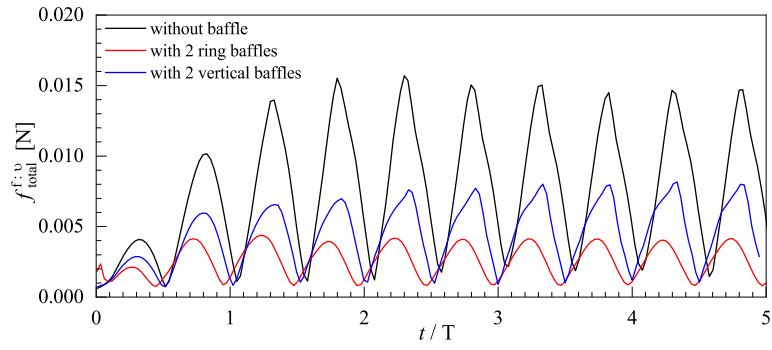
Figure 11: Vorticity distribution of three typical flow patterns. left: elastic tank without baffle, middle: elastic tank with 2 ring baffles, right: elastic tank with 2 vertical baffles.

head of the tanks. When the wave impacting, breaking and rolling occur in the tank without baffle, the vorticity in the corresponding fluid regions experiences rapid growth, producing apparent local maxima. However, upon the implementation of baffles, the distinctiveness of these typical phenomena diminishes, alongside a reduction in vorticity levels. The adoption of baffles in tanks appears to mitigate the prominence of these phenomena, effectively suppressing the rapid increase in vorticity observed in the absence of baffles.

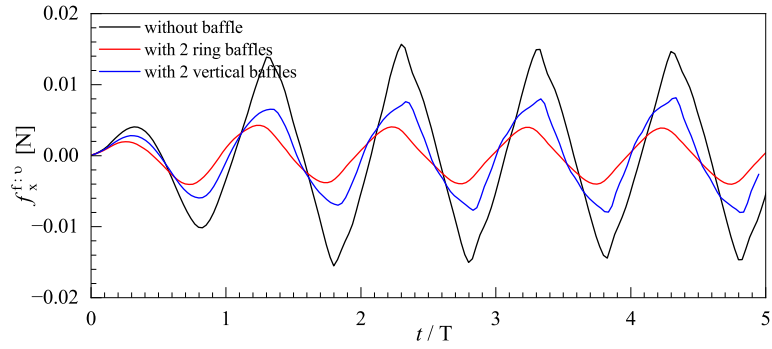
The viscous force and total force exerted on tank walls are depicted in Fig.12 and Fig.13. More intense waves are gradually generated and the forces on the solid walls exhibit periodic behavior after the initial period. The viscous force is a variable that intuitively reveals the flow state. The viscous component in the x direction accounts for the majority, since the horizontal sloshing mainly leads to the x-direction velocity of the fluid. The fluid in the tank without baffle is sloshing more violently causing a greater horizontal velocity and viscous force. Small viscous force $f_y^{f:\nu}$ initially indicates that there is negligible viscous friction caused by the flow in the y direction, suggesting the absence of swirl formation at the beginning. Following the simple sway motion, the emergence of breaking waves and swirling motion leads to a significant increase in $f_y^{f:\nu}$. As shown in Fig.13, the total force in the y direction plays a major role due to gravity. A distinct tendency emerges where baffles contribute to a reduction in the total load exerted on the tanks.

Illustrated in Fig.14 and Fig.15 are the distributions of the corresponding stress and strain distributions of tanks in the third period (sloshing stable stage). The central regions of both the front and rear walls, along with the bottoms of the standard LNG tank experience the highest levels of stress and distortion. As the fluid moves to the right and hits the head, a stress concentration zone appears in the lower right corner of the tank. These particular zones bear the brunt of the forces from the fluid under operating conditions. However, the installation of baffles into the tank design introduces a pivotal shift in how these stresses are distributed. These internal baffles alter the flow patterns of the fluid, and play a crucial role in alleviating the direct load on the main tank bodies by effectively deflecting the stress concentration domain onto themselves. The noteworthy decrease in stress and strain levels within the main bodies demonstrates the effectiveness of the baffle system in providing a more even distribution of forces throughout the tank interiors. Consequently, the tanks are better equipped to withstand the fluid impact without incurring undue wear and tear on the main structure.

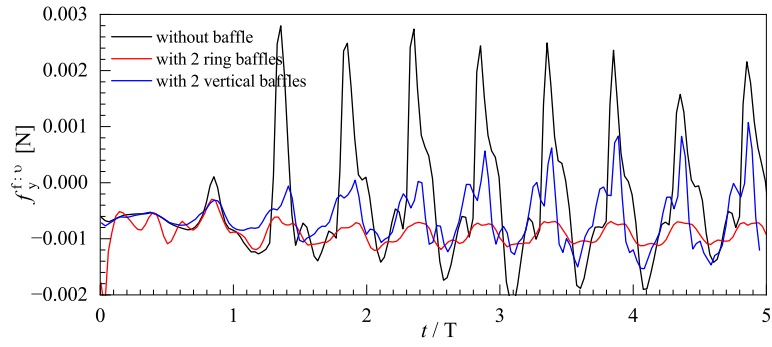
To facilitate a more detailed analysis of tank forces, the standard tank at $t = 3.38T$ is taken



(a)

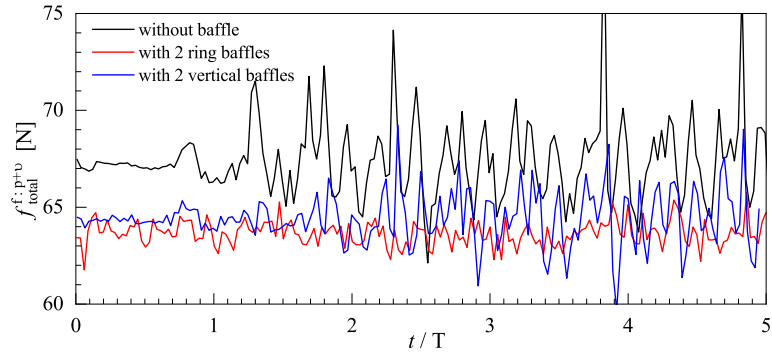


(b)

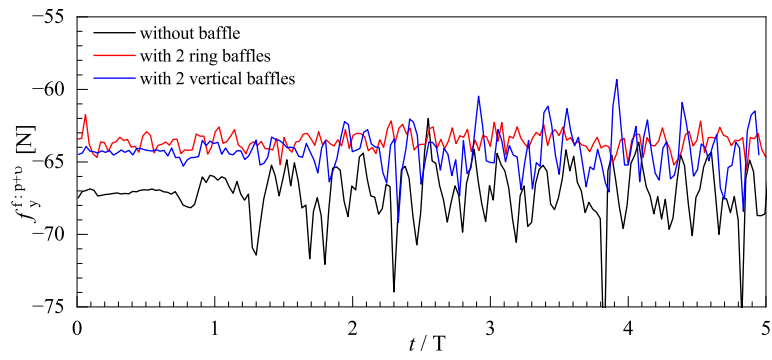


(c)

Figure 12: Comparison of viscous force on tank among normal tank, tank equipped with 2 ring baffles and tank equipped with 2 vertical baffles.



(a)



(b)

Figure 13: Comparison of total force on tank among normal tank, tank equipped with 2 ring baffles and tank equipped with 2 vertical baffles.

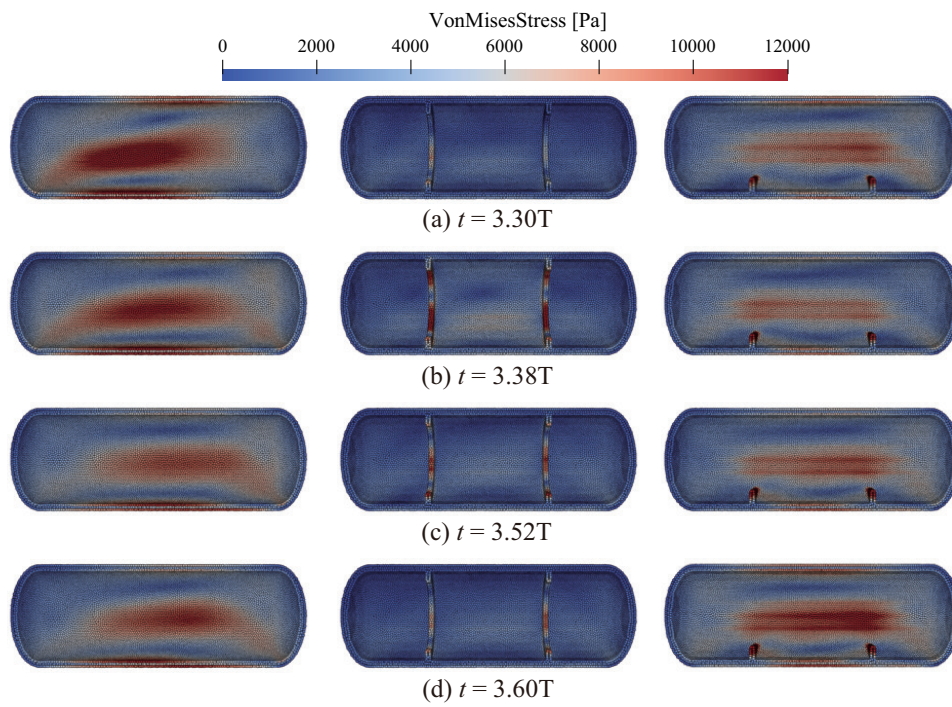


Figure 14: Stress distributions of tank in the third period. left: elastic tank without baffle, middle: elastic tank with 2 ring baffles, right: elastic tank with 2 vertical baffles.

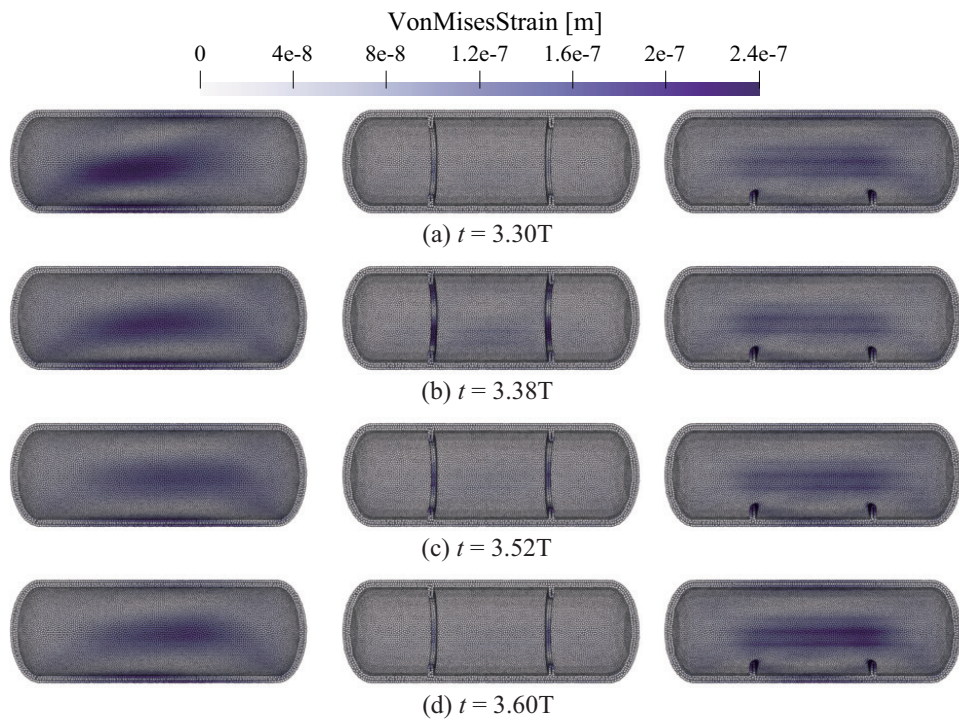


Figure 15: Strain distributions of tank in the third period. left: elastic tank without baffle, middle: elastic tank with 2 ring baffles, right: elastic tank with 2 vertical baffles.

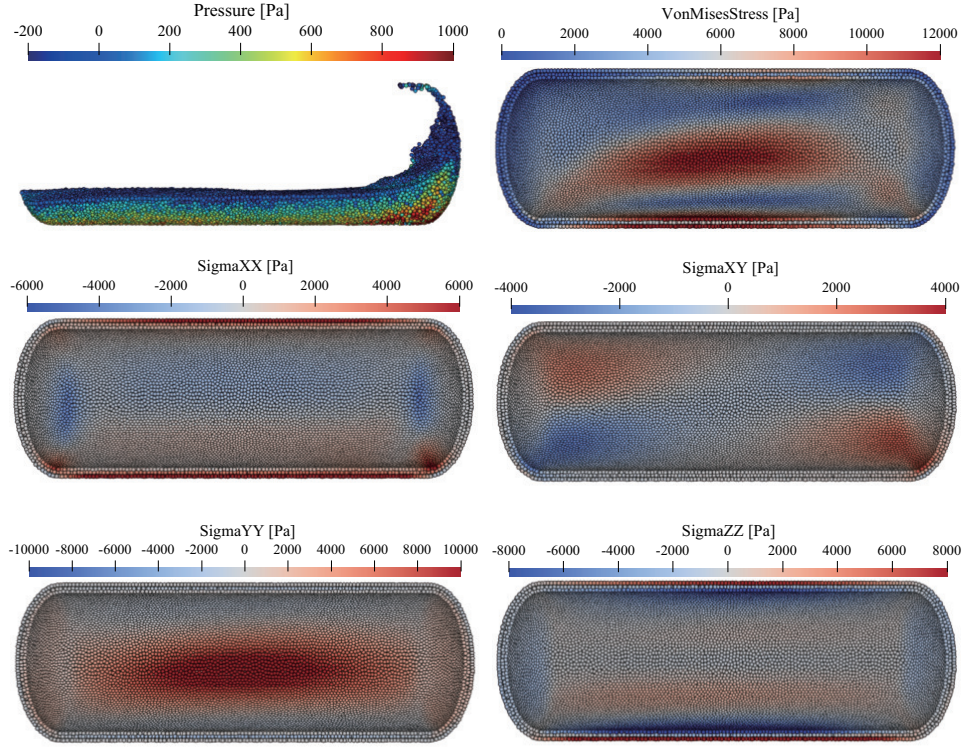


Figure 16: The stress distribution of elastic tank without baffle at $t = 3.38T$.

as an example to deconstruct the stress tensor matrix into its components: three normal stresses and three shear stresses. At this juncture, the fluid impacts the tank's right head, engendering a high-pressure zone in the lower right corner. Concurrently, the stress concentration on the tank walls migrates rightward, affected by the fluid's motion. The imposition of displacement constraints at the mass center of the tank and the influence of gravitational forces engender pronounced tensile stress along the vertical (y -axis) direction, and the horizontal (x -axis) direction, as well as the sectional (z -axis) direction, experience significant tensile stress across the tank's upper and lower external surfaces. Structural considerations further dictate that the normal stresses within the upper and lower internal walls of the z -axis direction exhibit marked compressive stress. Moreover, the velocity component of fluid sloshing introduces a shear stress gradient within the x - y plane, resulting in structural torsion.

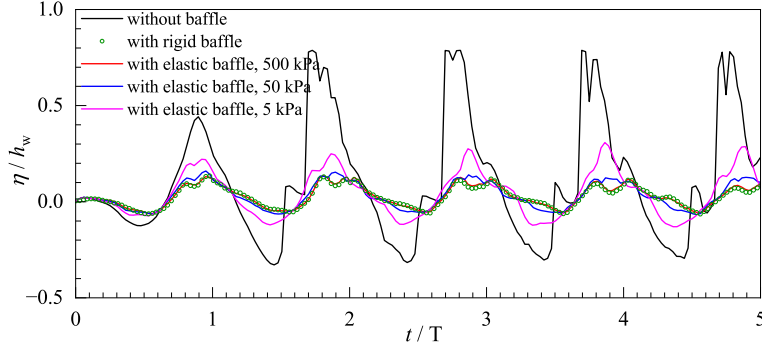


Figure 17: Comparison of non-dimensional free surface elevation of water among normal tank and tank with a rigid or elastic baffle.

5. Comparison between effects of rigid and elastic baffles

To compare the mitigation effect of rigid and elastic baffles on liquid sloshing, water depth $h_w/D = 0.5$ and a thicker wall with 0.03 m are used for modelling in this section, and a vertical baffle is inserted in the middle position. A rigid baffle or an elastic baffle is installed in the tank. The peripheral portion of the elastic baffle is fixed to the tank wall, and the Young's modulus of the elastic baffle is 500 kPa, 50 kPa or 5 kPa respectively. The physical properties of tank material remain the same as in the previous section, while the density and Poisson of elastic baffles are 2500 kg/m³ and 0.47.

Fig.17 shows the variation of free surface height during the first five periods, highlighting the critical role of baffles in suppressing large oscillations. However, when the Young's modulus of the elastic baffle is low, its effectiveness is limited. In other words, the closer the baffle's properties are to that of a rigid body, the stronger the inhibitory effect on liquid sloshing. As the Young's modulus reaches 500 kPa, there is a negligible difference in the performance between elastic and rigid baffles. The corresponding flow patterns of water including velocity and pressure distributions in various configurations at 2.25T and 2.5T are shown in Fig.18 and Fig.19, representing the fluid hitting the right head and the backflow. The velocity of the free surface is quite high in the tank without a baffle, while baffles substantially reduce the velocity magnitude, and have a certain effect on improving the high-pressure region of fluid near the tank corner. Also, it can be seen that the elastic baffle with Young's modulus equal to 5 kPa deforms under the impact of water, weakening its effectiveness in flow control.

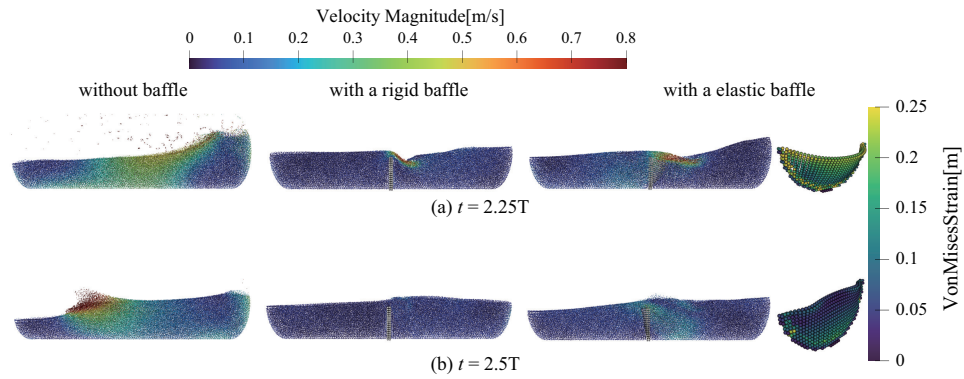


Figure 18: Fluid regimes of water in normal tank and tank with a rigid or elastic baffle (Young's modulus is 5 kPa) at $t = 2.25T$ and $t = 2.5T$. The right part is the strain distribution of the elastic baffle.

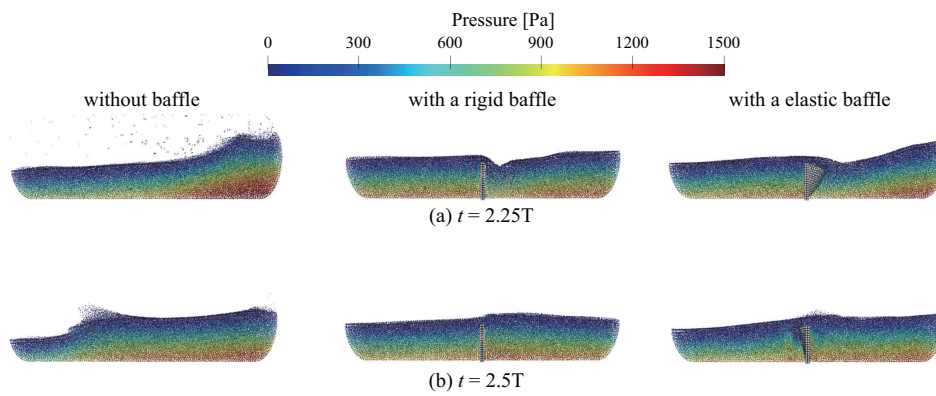


Figure 19: Pressure distribution of water in normal tank and tank with a rigid or elastic baffle at $t = 2.25T$ and $t = 2.5T$.

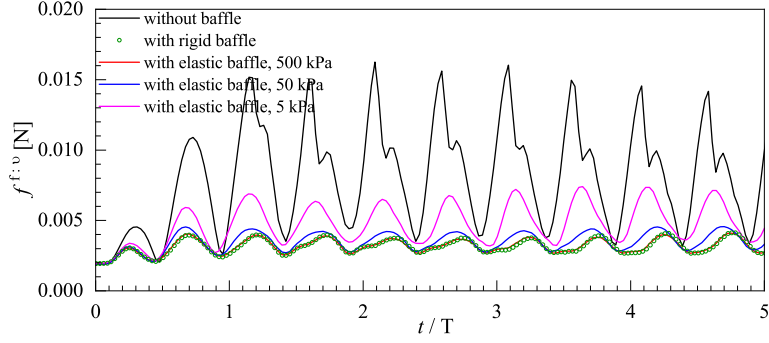


Figure 20: Viscous force on tank walls in normal tank and tank with a rigid or elastic baffle.

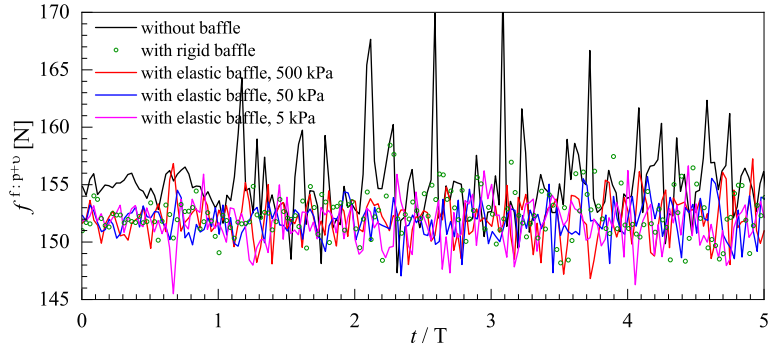


Figure 21: Total force on tank walls in normal tank and tank with a rigid or elastic baffle.

Fig.20 and Fig.21, depicting the viscous force and total force of the fluid on tanks, clearly illustrate that baffles have a remarkable effect on reducing the viscous force and total force on tanks. In addition, the distributions of stress and strain of tank walls at $t = 2.25T$ and $t = 2.5T$ are displayed in Fig.22 and Fig.23. The application of baffles results in a reduction in the maximum force and deformation range experienced by the tanks to a certain extent.

In the cases configured with various baffles, the viscous force and total force of fluid on the baffles are displayed in Fig.24 and Fig.25. The baffle with a smaller Young modulus exhibits a more pronounced variation in force over the course of the sloshing motion.

6. Conclusions

In the process of LNG transportation, attention should be paid to the load and deformation of the tanks with liquid sloshing to avoid structural damage. As a Lagrangian method, the numerical

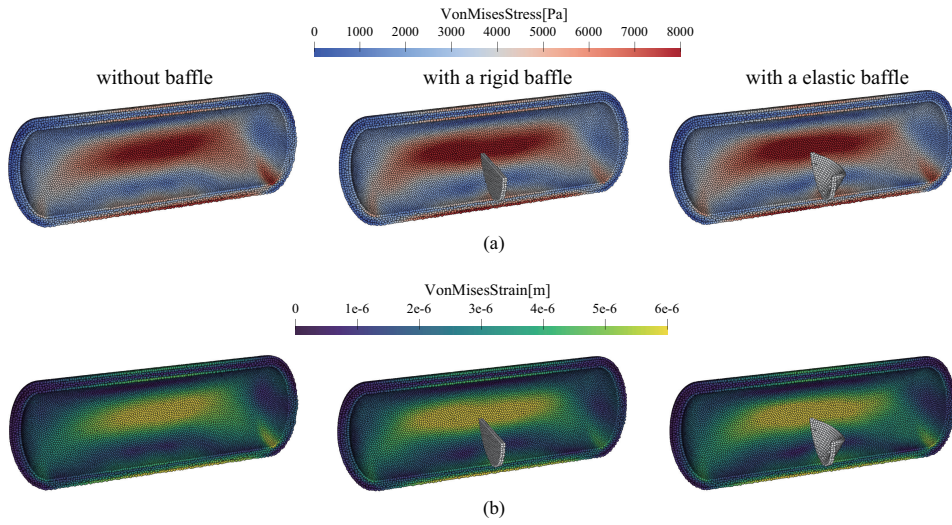


Figure 22: Stress and strain distributions of tanks at $t = 2.25T$.

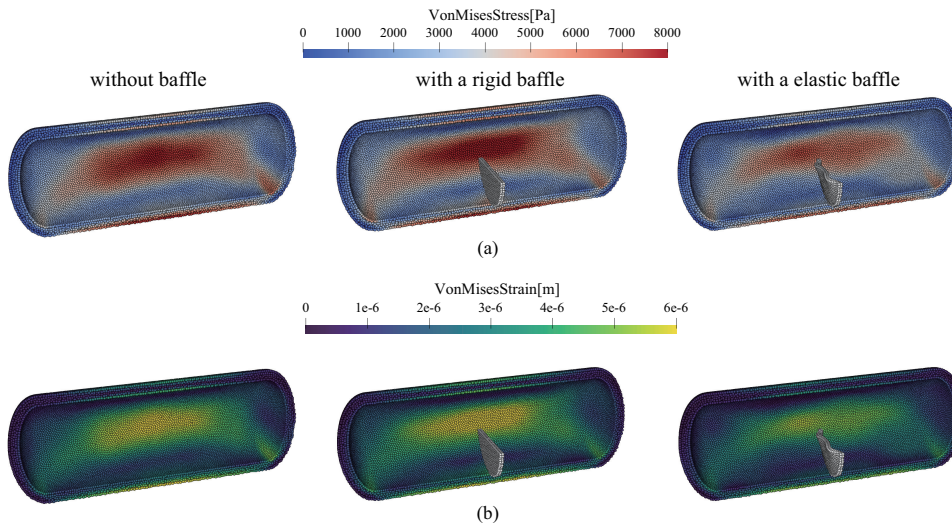


Figure 23: Stress and strain distributions of tanks at $t = 2.5T$.

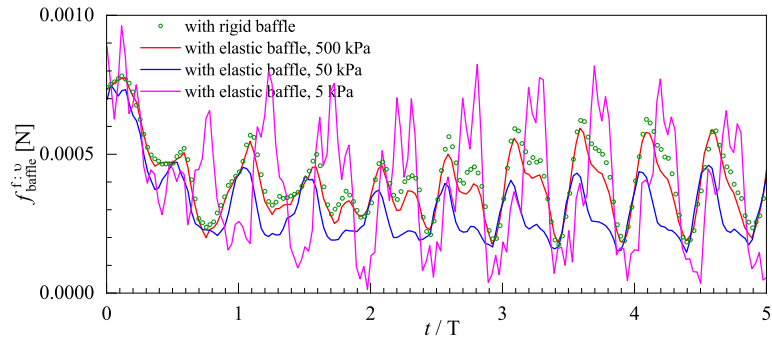


Figure 24: Viscous force on the baffle in tank with a rigid or elastic baffle.

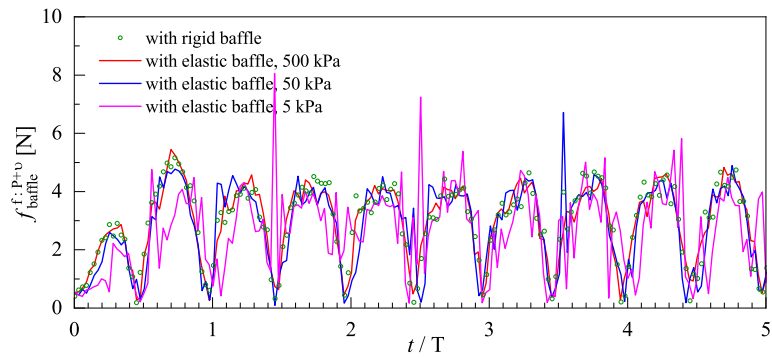


Figure 25: Total force on the baffle in tank with a rigid or elastic baffle.

research tool based on the SPH method employed in this paper serves as a reliable approach for handling the moving interface and free surface. It is necessary to model the tanks with elastic walls rather than rigid bodies, and the calculation of the interaction between fluid and solid within a single framework is adopted to reduce the error of data transfer and interpolation. In addition, the use of two-phase and three-dimensional modelling enhances the accuracy of the simulation. The performance of the current model is evaluated through the comparison between experimental data and numerical results, demonstrating its reliability. Consequently, this framework is adopted for the cases presented in this work to calculate the fluid dynamics for the flow fields and solid mechanics for the deformable structure.

The ring baffles and vertical baffles are applied to investigate their anti-sloshing effects and the variation of the force exerted on the tank walls by liquid sloshing. The introduction of baffles facilitates mitigating sloshing effectively by disrupting wave propagation, and in this comparison case, the ring baffles have a more pronounced effect in mitigating large oscillations. Examining the stress and strain distributions within the tanks reveals that due to the existence of baffles, concentration regions are shifted from the main tank bodies to the baffles, thereby reducing the risk of structural damage to the primary tank structure.

Finally, the rigid baffle and elastic baffles with several Young's moduli are inserted in the middle of the tank to investigate the influence of baffle material properties on sloshing inhibition. Numerical results indicate that baffle properties resembling those of a rigid body are more effective in suppressing liquid sloshing, resulting in a more noticeable improvement in the forces acting on the tank walls. This is because an elastic baffle with a high Young's modulus exhibits weaker control over fluid flow.

Acknowledgement

C.X. Zhao is fully supported by the China Scholarship Council (CSC) (No:202206280028). Y.C. Yu is fully supported by the China Scholarship Council (CSC) (No:201806120023). X.Y. Hu would like to express their gratitude to Deutsche Forschungsgemeinschaft for their sponsorship of this research under grant number DFG HU1572/10-1 and DFG HU1527/12-1.

CRedit authorship contribution statement

Chenxi Zhao: Investigation, Methodology, Visualization, Validation, Formal analysis, Writing - original draft, Writing - review & editing; **Yan Wu:** Investigation, Methodology, Validation; **Yongchuan Yu:** Investigation, Methodology; **Xiangyu Hu:** Supervision, Methodology, Writing - review & editing; **Oskar J. Haidn:** Supervision.

Declaration of competing interest

The authors declare that they have no known competing financial interests or personal relationships that could have appeared to influence the work reported in this paper.

Data availability

The code is open source on <https://www.sphinxsys.org>.

References

- [1] E. L. Grotle, V. Æsøy, Experimental and numerical investigation of sloshing in marine lng fuel tanks, in: International Conference on Offshore Mechanics and Arctic Engineering, Vol. 57632, American Society of Mechanical Engineers, 2017, p. V001T01A046.
- [2] G. Liu, Y. Lin, G. Guan, Y.-y. Yu, Numerical research on the anti-sloshing effect of a ring baffle in an independent type c lng tank, *Journal of Zhejiang University-Science A* 19 (10) (2018) 758–773.
- [3] M. A. Goudarzi, S.-R. Sabbagh-Yazdi, W. Marx, Investigation of sloshing damping in baffled rectangular tanks subjected to the dynamic excitation, *Bulletin of Earthquake Engineering* 8 (2010) 1055–1072.
- [4] M.-a. Xue, P.-z. Lin, J.-h. Zheng, Y.-x. Ma, X.-l. Yuan, V.-T. Nguyen, Effects of perforated baffle on reducing sloshing in rectangular tank: experimental and numerical study, *China Ocean Engineering* 27 (2013) 615–628.
- [5] H. Jin, Y. Liu, H.-J. Li, Experimental study on sloshing in a tank with an inner horizontal perforated plate, *Ocean Engineering* 82 (2014) 75–84.
- [6] T. Nasar, S. Sannasiraj, Sloshing dynamics and performance of porous baffle arrangements in a barge carrying liquid tank, *Ocean Engineering* 183 (2019) 24–39.
- [7] A. M. Aly, M. T. Nguyen, S.-W. Lee, Numerical analysis of liquid sloshing using the incompressible smoothed particle hydrodynamics method, *Advances in Mechanical Engineering* 7 (2) (2015) 765741.
- [8] O. M. Faltinsen, A nonlinear theory of sloshing in rectangular tanks, *Journal of Ship Research* 18 (04) (1974) 224–241.
- [9] O. M. Faltinsen, A numerical nonlinear method of sloshing in tanks with two-dimensional flow, *Journal of Ship Research* 22 (03) (1978) 193–202.
- [10] J. Cho, H. Lee, Numerical study on liquid sloshing in baffled tank by nonlinear finite element method, *Computer methods in applied mechanics and engineering* 193 (23-26) (2004) 2581–2598.

- [11] K. Biswal, S. Bhattacharyya, P. Sinha, Non-linear sloshing in partially liquid filled containers with baffles, *International Journal for Numerical Methods in Engineering* 68 (3) (2006) 317–337.
- [12] Y. Kim, Numerical simulation of sloshing flows with impact load, *Applied Ocean Research* 23 (1) (2001) 53–62.
- [13] B.-F. Chen, R. Nokes, Time-independent finite difference analysis of fully non-linear and viscous fluid sloshing in a rectangular tank, *Journal of Computational Physics* 209 (1) (2005) 47–81.
- [14] M.-A. Xue, P. Lin, Numerical study of ring baffle effects on reducing violent liquid sloshing, *Computers & Fluids* 52 (2011) 116–129.
- [15] K.-J. Paik, P. M. Carrica, Fluid–structure interaction for an elastic structure interacting with free surface in a rolling tank, *Ocean Engineering* 84 (2014) 201–212.
- [16] U. O. Ünal, G. Bilici, H. Akyıldız, Liquid sloshing in a two-dimensional rectangular tank: A numerical investigation with a t-shaped baffle, *Ocean Engineering* 187 (2019) 106183.
- [17] K. Threepopnartkul, C. Suvanjumrat, The effect of baffles on fluid sloshing inside the moving rectangular tank, *Journal of Research and Applications in Mechanical Engineering* 1 (2) (2012) 37–42.
- [18] J. R. Saripilli, D. Sen, Numerical studies on effects of slosh coupling on ship motions and derived slosh loads, *Applied Ocean Research* 76 (2018) 71–87.
- [19] C. Yang, R. Niu, P. Zhang, Numerical analyses of liquid slosh by finite volume and lattice boltzmann methods, *Aerospace Science and Technology* 113 (2021) 106681.
- [20] Y.-y. Tang, Y.-d. Liu, C. Chen, Z. Chen, Y.-p. He, M.-m. Zheng, Numerical study of liquid sloshing in 3d lng tanks with unequal baffle height allocation schemes, *Ocean Engineering* 234 (2021) 109181.
- [21] M.-A. Xue, O. Kargbo, J. Zheng, Seiche oscillations of layered fluids in a closed rectangular tank with wave damping mechanism, *Ocean Engineering* 196 (2020) 106842.

- [22] S.-C. Hwang, J.-C. Park, H. Gotoh, A. Khayyer, K.-J. Kang, Numerical simulations of sloshing flows with elastic baffles by using a particle-based fluid-structure interaction analysis method, *Ocean Engineering* 118 (2016) 227–241.
- [23] X. Cao, F. Ming, A. Zhang, Sloshing in a rectangular tank based on sph simulation, *Applied Ocean Research* 47 (2014) 241–254.
- [24] A. George, I. Cho, Anti-sloshing effects of a vertical porous baffle in a rolling rectangular tank, *Ocean Engineering* 214 (2020) 107871.
- [25] P. Nimisha, B. Jayalekshmi, K. Venkataramana, Effective configuration of perforated baffle plate for efficient slosh damping in liquid retaining tanks under lateral excitation, *Ocean Engineering* 259 (2022) 111855.
- [26] A. Zhu, M.-A. Xue, X. Yuan, F. Zhang, W. Zhang, Effect of double-side curved baffle on reducing sloshing in tanks under surge and pitch excitations, *Shock and Vibration* 2021 (2021) 1–17.
- [27] A. Trimulyono, H. Atthariq, D. Chrismianto, S. Samuel, Investigation of sloshing in the prismatic tank with vertical and t-shape baffles, *Brodogradnja: Teorija i praksa brodogradnje i pomorske tehnike* 73 (2) (2022) 43–58.
- [28] M.-A. Xue, J. Zheng, P. Lin, et al., Numerical simulation of sloshing phenomena in cubic tank with multiple baffles, *Journal of Applied Mathematics* 2012 (2012).
- [29] D. Lee, M. Kim, S. Kwon, J. Kim, Y. Lee, A parametric sensitivity study on lng tank sloshing loads by numerical simulations, *Ocean Engineering* 34 (1) (2007) 3–9.
- [30] L. Delorme, A. Colagrossi, A. Souto-Iglesias, R. Zamora-Rodriguez, E. Botia-Vera, A set of canonical problems in sloshing, part i: Pressure field in forced roll—comparison between experimental results and sph, *Ocean Engineering* 36 (2) (2009) 168–178.
- [31] A. Al-Zughaibi, E. Hussein, F. Rashid, A dynamic meshing technique for analysis of nonlinear sloshing in liquid tanks, in: *IOP Conference Series: Materials Science and Engineering*, Vol. 1067, IOP Publishing, 2021, p. 012094.

- [32] H. Akyildiz, E. Ünal, Experimental investigation of pressure distribution on a rectangular tank due to the liquid sloshing, *Ocean Engineering* 32 (11-12) (2005) 1503–1516.
- [33] Z.-Y. Fang, M.-Y. Duan, R.-Q. Zhu, Numerical simulation of liquid sloshing in a liquid tank based on level-set method., *Chuanbo Lixue(Journal of Ship Mechanics)* 11 (1) (2007) 62–67.
- [34] S. Li, W. K. Liu, Meshfree and particle methods and their applications, *Appl. Mech. Rev.* 55 (1) (2002) 1–34.
- [35] T. Ye, D. Pan, C. Huang, M. Liu, Smoothed particle hydrodynamics (sph) for complex fluid flows: Recent developments in methodology and applications, *Physics of Fluids* 31 (1) (2019).
- [36] J. Shao, H. Li, G. Liu, M. Liu, An improved sph method for modeling liquid sloshing dynamics, *Computers & Structures* 100 (2012) 18–26.
- [37] Z. Zhang, M. Khalid, T. Long, M. Liu, C. Shu, Improved element-particle coupling strategy with δ -sph and particle shifting for modeling sloshing with rigid or deformable structures, *Applied Ocean Research* 114 (2021) 102774.
- [38] Y. Ren, A. Khayyer, P. Lin, X. Hu, Numerical modeling of sloshing flow interaction with an elastic baffle using sphxsys, *Ocean Engineering* 267 (2023) 113110.
- [39] C. Pilloton, A. Bardazzi, A. Colagrossi, S. Marrone, Sph method for long-time simulations of sloshing flows in lng tanks, *European Journal of Mechanics-B/Fluids* 93 (2022) 65–92.
- [40] A. Trimulyono, H. Hashimoto, A. Matsuda, Experimental validation of single-and two-phase smoothed particle hydrodynamics on sloshing in a prismatic tank, *Journal of Marine Science and Engineering* 7 (8) (2019) 247.
- [41] K. Liao, C. Hu, A coupled fdm–fem method for free surface flow interaction with thin elastic plate, *Journal of marine science and technology* 18 (2013) 1–11.
- [42] G. Zhang, W. Zhao, D. Wan, Partitioned mps-fem method for free-surface flows interacting with deformable structures, *Applied Ocean Research* 114 (2021) 102775.
- [43] Q. Yang, V. Jones, L. McCue, Free-surface flow interactions with deformable structures using an sph–fem model, *Ocean engineering* 55 (2012) 136–147.

- [44] Z. Zhang, M. Khalid, T. Long, J. Chang, M. Liu, Investigations on sloshing mitigation using elastic baffles by coupling smoothed finite element method and decoupled finite particle method, *Journal of Fluids and Structures* 94 (2020) 102942.
- [45] T. Hu, S. Wang, G. Zhang, Z. Sun, B. Zhou, Numerical simulations of sloshing flows with an elastic baffle using a sph-spim coupled method, *Applied Ocean Research* 93 (2019) 101950.
- [46] C. Zhang, M. Rezavand, Y. Zhu, Y. Yu, D. Wu, W. Zhang, J. Wang, X. Hu, Sphinxsys: An open-source multi-physics and multi-resolution library based on smoothed particle hydrodynamics, *Computer Physics Communications* 267 (2021) 108066.
- [47] M. Antuono, A. Colagrossi, S. Marrone, Numerical diffusive terms in weakly-compressible sph schemes, *Computer Physics Communications* 183 (12) (2012) 2570–2580.
- [48] M. Rezavand, C. Zhang, X. Hu, A weakly compressible sph method for violent multi-phase flows with high density ratio, *Journal of Computational Physics* 402 (2020) 109092.
- [49] X. Y. Hu, B. C. Khoo, An interface interaction method for compressible multifluids, *Journal of Computational Physics* 198 (1) (2004) 35–64.
- [50] C. Zhang, X. Hu, N. A. Adams, A weakly compressible sph method based on a low-dissipation riemann solver, *Journal of Computational Physics* 335 (2017) 605–620.
- [51] S. Adami, X. Hu, N. A. Adams, A transport-velocity formulation for smoothed particle hydrodynamics, *Journal of Computational Physics* 241 (2013) 292–307.
- [52] C. Zhang, X. Y. Hu, N. A. Adams, A generalized transport-velocity formulation for smoothed particle hydrodynamics, *Journal of Computational Physics* 337 (2017) 216–232.
- [53] S. Adami, X. Y. Hu, N. A. Adams, A generalized wall boundary condition for smoothed particle hydrodynamics, *Journal of Computational Physics* 231 (21) (2012) 7057–7075.
- [54] M. Rezavand, C. Zhang, X. Hu, Generalized and efficient wall boundary condition treatment in gpu-accelerated smoothed particle hydrodynamics, *Computer Physics Communications* 281 (2022) 108507.
- [55] R. Vignjevic, J. R. Reveles, J. Campbell, Sph in a total lagrangian formalism, *CMC-Tech Science Press- 4* (3) (2006) 181.

- [56] C. Zhang, M. Rezavand, X. Hu, A multi-resolution sph method for fluid-structure interactions, *Journal of Computational Physics* 429 (2021) 110028.
- [57] Y. Zhu, C. Zhang, X. Hu, A dynamic relaxation method with operator splitting and random-choice strategy for sph, *Journal of Computational Physics* 458 (2022) 111105.
- [58] C. Zhang, M. Rezavand, X. Hu, Dual-criteria time stepping for weakly compressible smoothed particle hydrodynamics, *Journal of Computational Physics* 404 (2020) 109135.